

Bottom-up and top-down reasoning with convolutional latent-variable models

Peiyun Hu
UC Irvine

peiyunh@ics.uci.edu

Deva Ramanan
UC Irvine

dramanan@ics.uci.edu

Abstract

Convolutional neural nets (CNNs) have demonstrated remarkable performance in recent history. Such approaches tend to work in a “unidirectional” bottom-up feed-forward fashion. However, biological evidence suggests that feedback plays a crucial role, particularly for detailed spatial understanding tasks. This work introduces “bidirectional” architectures that also reason with top-down feedback: neural units are influenced by both lower and higher-level units. We do so by treating units as latent variables in a global energy function. We call our models convolutional latent-variable models (CLVMs). From a theoretical perspective, CLVMs unify several approaches for recognition, including CNNs, generative deep models (e.g., Boltzmann machines), and discriminative latent-variable models (e.g., DPMs).

From a practical perspective, CLVMs are particularly well-suited for multi-task learning. We describe a single architecture that simultaneously achieves state-of-the-art accuracy for tasks spanning both high-level recognition (part detection/localization) and low-level grouping (pixel segmentation). Bidirectional reasoning is particularly helpful for detailed low-level tasks, since they can take advantage of top-down feedback. Our architectures are quite efficient, capable of processing an image in milliseconds. We present results on benchmark datasets with both part/keypoint labels and segmentation masks (such as PASCAL and LFW) that demonstrate a significant improvement over prior art, in both speed and accuracy.

1. Introduction

Convolutional neural nets (CNN’s), pioneered by LeCun *et al.* [33], have demonstrated remarkable performance in recent history [29, 42, 45]. One attractive property is their ability to transfer knowledge across tasks: CNN’s trained for image classification perform well for object detection [8], image captioning [26], and pose estimation [4], among other tasks [39]. Often, this requires a small amount of fine-tuning. A tantalizing question is whether a single universal “off-the-shelf” feature extractor could support a

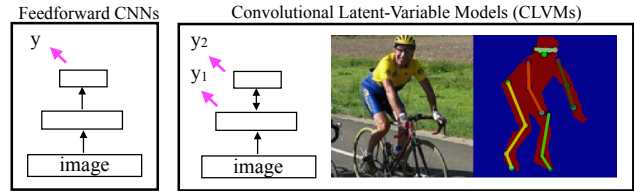


Figure 1: Traditional feed-forward neural architectures produce a target prediction for a high-level task (such as image classification) using features extracted from a high neural layer (**left**). We introduce latent variable models that incorporate top-feedback, where lower variable activations are influenced by higher variables. Such architectures can produce state-of-the-art features for high-level tasks (like keypoint detection/localization) and low-level tasks (like pixel segmentation). We show an example of predictions for both keypoint localization (visualized as a skeleton) and pixel-segmentation on the **right** image.

wide range of tasks from high-level recognition to low-level pixel grouping.

Feedback: Human physiology provides strong evidence for the existence of such a universal feature hierarchy [30]. Rapid response times for coarse recognition tasks [47] suggest that the hierarchy is computed in a feed-forward fashion. However, when subjects are asked to disambiguate fine-grained categories [27] or perform detailed spatial tasks [21], feedback appears to play a vital role. For example, low-level V1 neurons tuned for local features (such as oriented edges) can adapt to a global figure-ground mask after 40ms [32, 56]. Indeed, biological evidence suggests that *most* neural connections in the brain are feedback rather than feedforward [5, 30]. We take away two conclusions from these observations: (1) a universal architecture capable of both high and low-level tasks will likely require feedback and (2) feedback occurs fairly rapidly (within 100ms).

Boltzmann machines: To begin our discussion, we appeal to mathematical models that *are* capable of bidirectional reasoning. One elegant approach is that of hierarchical probabilistic models [22, 34, 54]. Boltzmann ma-

chines [1] can be seen as the generative probabilistic deep “counterpart” to CNNs. Importantly, neural units in deep Boltzmann machines are influenced by those in layers below *and above* [40]. The basic mechanism for accomplishing this is a (normalized) global energy function linking all units together. Though quite attractive, such models have not enjoyed the empirical success of discriminatively-trained, feed-forward counterparts.

Part models: In principle, global energy (or scoring) functions could be trained discriminatively. This is the basis for much of structured prediction, including the widely-used deformable part model (DPM) [6]. Interestingly, feed-forward inference on DPMs can be written as a CNN [9]. But our interest in DPMs stems their ability for top-down feedback: a high-level “root” object can influence the activation of a lower-level “part”. Such models were state-of-the-art until recently, but appear to have saturated because learning deep hierarchies of parts remains challenging.

Overview: We introduce a convolutional latent variable model (CLVM) that unifies these representations. CLVMs are defined over a global scoring function (like a Boltzmann machine), but with convolutionally tied weights (like a CNN). The global scoring function is *not* probabilistic normalized, and instead is discriminatively trained with supervision (like a DPM). Crucially, CLVMs can be implemented with modifications to existing deep learning toolboxes, allowing one to make use of highly optimized routines for gradient-based learning. After describing our model in detail, we compare it to related work in deep learning in Sec. 2.

Related work: (joint recognition and grouping) There has been a considerable amount of work integrating high-level recognition with low-level grouping cues. One approach is top-down guided segmentation: for example, one can prime a low-level pixel segmentation engine with top-down cues from an object detector [2, 3, 31, 51]. Other approaches use bottom-up proposals to prime object detections [8, 13]. In either case, recognition and grouping steps are typically treated as separate stages in a pipeline, making it difficult to perform end-to-end multi-task training (unlike CLVMs).

2. Latent variable model

In this section, we introduce our convolutional latent-variable models (CLVMs). We begin with a high-level overview. Variables will be organized into layers, spatial locations, and channels (much like the neural activations of a CNN). CLVMs are optimized by layer-wise coordinate descent through convolution, rectification, and max-pooling operations. These operations are similar to those in contemporary CNNs, but crucially differ in that they allow for top-down feedback. We will explore the theoretical relationship between CNNs and CLVMs in detail.

To begin our discussion, let us recall the central *neurody-*

namic equation governing the activation of a single “neural unit” z_i [15]:

$$z_i = \phi(b_i + \sum_{j \neq i} w_{ij} z_j) \quad (1)$$

where b_i is a bias, w_{ij} are weights between units i and j that define excitatory or inhibitory interactions depending on their sign and magnitude. Importantly, ϕ is a non-linear activation function. Ackley *et al.* [1] point out that when the activation is a sigmoid function, (1) can be seen as stochastic updates for a global probabilistic model known as a Boltzmann machine:¹

$$\begin{aligned} \phi_{sig}(x) &= \frac{1}{1 + e^{-x}} \Rightarrow P(z) \propto e^{S_{Boltz}(z)} \quad \text{where} \\ S_{Boltz}(z) &= \frac{1}{2} z^T W z + b^T z, \quad z_i \in \{0, 1\}, w_{ii} = 0 \end{aligned} \quad (2)$$

where $W = [w_{ij}]$, $z = [z_i]$, and $b = [b_i]$. Here, units z are treated as binary latent variables that capture the absence or presence of various features. Importantly, these variables are linked in a globally consistent scoring function that captures bidirectional interactions between variables encoded in the symmetric matrix W . This coupling allows low-level features (e.g., edges) to effect high-level features (e.g., objects) and vice-versa. While conceptually attractive, such models are difficult to train in practice, typically requiring sampling approximations such as contrastive divergence [16].

Let us replace the sigmoid with a simple rectified linear activation (common in contemporary deep models [10, 37]). We will show that associated neural updates correspond to coordinate descent optimization of a global scoring function that is similar to $S_{Boltz}(z)$:

$$\begin{aligned} z_i &= \max(0, b_i + \sum_{j \neq i} w_{ij} z_j) \Rightarrow \max_{z \geq 0} S(z) \quad \text{where} \\ S(z) &= \frac{1}{2} z^T W z + b^T z, \quad z_i \in R^+, w_{ii} = -1 \end{aligned} \quad (3)$$

There are two important differences between $S(z)$ and $S_{Boltz}(z)$. First, latent variables z are no longer binary, but non-negative real numbers. Intuitively, they can be interpreted as capturing the absence or presence of a feature, and if present, the strength of its activation (possibly encoding the firing rate of a neuron [25]). Second, a quadratic term is added to the diagonal of W that acts as a regularizer, penalizing large activations of z . (3) is a quadratic function subject to non-negativity constraints, which is readily recognized as a quadratic program (QP). When $-W$ is positive semi-definite (PSD), the above QP can be written as a *non-negative least squares optimization* $\min_{z \geq 0} \frac{1}{2} \|Az - y\|$

¹One can derive deterministic Boltzmann machine updates of the form from (1) using mean-field variational inference algorithms [23, 38].

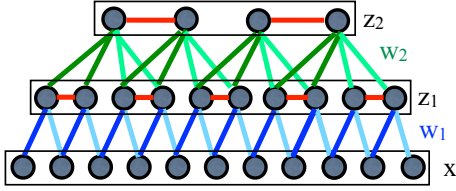


Figure 2: A convolutional latent-variable model (CLVM). We visualize latent variables with circles, that are arranged into layers and spatial locations. We write x for the input image, z_i for latent variables from layer i , w_i for convolutional weights connecting layer $i - 1$ to i . We draw lateral inhibitory connections between latent variables within a pooling window in red. Layer-wise coordinate descent updates on this model can be computed by CNN operations of filtering, rectification, and max-pooling.

where $-W = A^T A$ and $b = A^T y$, implying a globally optimal solution exists. When $-W$ is strictly positive definite, the solution must be unique.

Inference: Let us optimize (3) with coordinate descent, solving for a single z_i holding all others fixed. Maximizing a 1-d quadratic function subject to non-negative constraints is easily done by solving for the optimum and clipping:

$$\begin{aligned} \max_{z_i > 0} f(z_i) \quad \text{where} \quad f(z_i) &= -\frac{1}{2}z_i^2 + (b_i + \sum_{j \neq i} w_{ij}z_j)z_i \\ \frac{\partial f}{\partial z_i} &= -z_i + b_i + \sum_{j \neq i} w_{ij}z_j = 0 \\ z_i &= \max(0, b_i + \sum_{j \neq i} w_{ij}z_j) \end{aligned} \quad (4)$$

where (4) is exactly equivalent to (1) for a rectified linear activation. When $-W$ is PSD, the above coordinate descent updates must converge to an optimal solution [7].

Inference with CNNs: We will show that state-of-the-art CNN architectures [42] actually perform coordinate-wise updates of the form from (4). With a slight abuse of notation, we denote the latent variable at layer i corresponding to spatial position u as $z_i[u]$. We denote the weight connecting $z_{i-1}[u]$ to $z_i[v]$ as $w_i[\tau]$, where $\tau = u - v$ depends only on the relative offset between u, v :

$$z_i[u] = \max(0, b_i + \text{top}_i[u] + \text{bot}_i[u]) \quad \text{where} \quad (5)$$

$$\text{top}_i[u] = \sum_{\tau} w_{i+1}[\tau]z_{i+1}[u - \tau]$$

$$\text{bot}_i[u] = \sum_{\tau} w_i[\tau]z_{i-1}[u + \tau]$$

where we assume that layers have a single one-dimensional channel of a fixed length to simplify notation. By tying together weights such that they only depend on relative

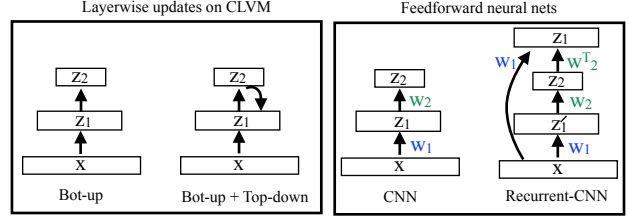


Figure 3: On the **left**, we visualize two sequences of layer-wise coordinate updates on our latent-variable model. The first is a bottom-up pass, while the second is a bottom-up + top-down pass. On the **right**, we show that bottom-up updates can be *exactly* computed with a feed-forward CNN, and bottom-up-and-top-down updates can be *exactly* computed with an “unrolled” CNN with additional skip connections and tied weights (which we define as a recurrent CNN). We use T to denote a 180 degree rotation of filters that maps correlation to convolution. We follow the color scheme from Fig. 2.

locations, bottom-up signals can be computed with cross-correlational filtering, while top-down signals can be computed with convolution. In the existing literature, these are sometimes referred to as deconvolutional and convolutional filters (related through a 180 rotation) [53]. It is natural to start coordinate updates from the bottom layer z_1 , initializing all variables to 0. During the initial bottom-up coordinate pass, top_i will always be 0. This means that the bottom-up coordinate updates can be computed with simple filtering and thresholding. *Hence a single bottom-up pass of layer-wise coordinate optimization of a CLVM can be implemented with a CNN.*

Top-down feedback: We add top-down feedback simply by applying additional coordinate updates (5) in a top-down fashion, from the top-most layer to the bottom. Fig. 3 shows that such a sequence of bottom-up and top-down updates can be “unrolled” into a feed-forward CNN with “skip” connections between layers and tied weights. One can interpret such a model as a recurrent CNN that is capable of feedback, since lower-layer variables (capturing say, edges) can now be influenced by the activations of high-layer variables (capturing say, objects). If the associated weight matrix is PSD, an infinitely-deep unrolled CNN *must* converge to a globally-optimal solution (because of the equivalence to a non-negative least squares optimization).

Non-maximal suppression (NMS): To encourage sparse activations, we add lateral inhibitory connections between groups of variables in a layer. Specifically, we write the weight connecting $z_i[u]$ and $z_i[v]$ for $(u, v) \in \text{group}$ as $w_i[u, v] = -\infty$. Such connections are shown as red edges in Fig. 2. When groups are disjoint (say, non-overlapping 2×2 windows), *layer-wise updates can be im-*

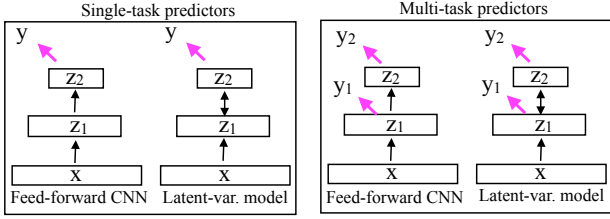


Figure 4: On the **left**, we contrast two models for single-task prediction: feed-forward CNNs versus bidirectional CLVMs (capable of top-down feedback). On the **right**, we visualize multi-task predictive models, tuned for both high-level tasks (such as part detection) and low-level tasks (such as pixel segmentation). We show that bidirectional models excel at multi-task prediction because lower-layer features become more accurate with feedback.

plemented by applying (5) (filtering and rectification) followed by max’ing within each group. Our NMS operation differs from max-pooling in that it returns 0 values for non-maximal locations (and so encodes the spatial location of the maximum). Interestingly, CNNs that use non-overlapping pooling windows [42] can be written as a special case where filter weights w_{i+1} are replicated across variables z_i in the same pooling window (as shown in Fig. 2). This makes NMS independent of the top-down signal top_i . However, our architecture is more general in that NMS is guided by top-down feedback: high-level variables (capturing objects) can influence both the activation and spatial location of low-level variables (capturing edges). Our simple approach retains detailed spatial information, which appears difficult to capture in traditional CNNs [17].

Approximate inference: Given the above global scoring function and an image x , inference corresponds to $\text{argmax}_z S(x, z)$. As argued above, this can be implemented with an infinitely-deep unrolled recurrent CNN. However, rather than optimizing the latent variables to completion, we perform a fixed number (k) of layer-wise coordinate descent updates. This is guaranteed to report back finite variables z^* even when the associated weight matrix is not PSD (implying the true solution is unbounded):

$$z^* = \mathbf{CLVM}_k(x, W, b), \quad z^* \in R^N \quad (6)$$

We write \mathbf{CLVM}_k in bold to emphasize that it is a *vector-valued function* implementing k passes of layer-wise coordinate descent, returning a vector of all N latent variables. We set $k = 1$ for a single bottom-up pass (corresponding to a standard feed-forward CNN) and $k = 2$ for an additional top-down pass.

Output prediction: We will use these N variables as features for M different tasks that span both low-level (such as pixel segmentation) and high-level tasks (such as part lo-

calization) - see Fig. 4. Because our latent variables serve as rich, multiscale description of image features, we assume that simple linear predictors built on them will suffice:

$$y = Vz^*, \quad y \in R^M, V \in R^{M \times N} \quad (7)$$

Training: Our overall model is parameterized by (W, V, b) . Assume we are given training data pairs of images and output label vectors $\{x_i, y_i\}$. We define a training objective as follows

$$\min_{W, V, b} R(W) + R(V) + \sum_i \text{loss}(y_i, V\mathbf{CLVM}_k(x_i, W, b)) \quad (8)$$

where R are regularizer functions (we use the Frobenius matrix norm) and “loss” sums the loss of our M prediction tasks (where each is scored with log or softmax loss). We optimize the above by stochastic gradient descent. Because \mathbf{CLVM}_k is a deterministic function, its gradient with respect to (W, b) can be computed by backpropagation on the k -times unrolled recurrent CNN (Fig. 3). We separate V from W to ensure that feature extraction does not scale with the number of output tasks (\mathbf{CLVM}_k is independent of M). During learning, we fix diagonal weights ($w_i[u, u] = -1$) and lateral inhibition weights ($w_i[u, v] = -\infty$ for $(u, v) \in \text{group}$).

Related work (learning): The use of gradient-based backpropagation to learn an unrolled model dates back to ‘backprop-through-structure’ algorithms [11, 43] and graph transducer networks [33]. More recently, such approaches were explored general graphical models [44] and Boltzmann machines [12]. Our work uses such ideas to learn CNNs with top-down feedback using an unrolled latent-variable model. Unlike past work, our latent-variable model (3) captures ReLU activations (crucial for high-performance [29]) and provides formal guarantees of optimality (for a PSD weight matrix).

Related work (top-down): Related CNN architectures capturing top-down feedback include “fully-convolutional” networks [35] (which combine cues across multiple layers through upsampling) and deconvolutional networks (which can visualize top-down activations) [52]. While those networks tend to be empirically motivated, we theoretically derive the “right” network corresponding to a latent-variable model. Crucially, our network allows for nonlinear operations (rectification and max-pooling) to be influenced by top-down knowledge (5), unlike [35, 52]. From this perspective, our network relates to neural autoencoders that reconstruct an image given top-down cues estimated in a “bottleneck” layer [18, 36, 49], but our network explicitly adds a bottom-up component (the skip connection in Fig. 3).

the layer and filter size for all models separately. We find that 5×5 filters work consistently well. For $CLVM_1$ and $M-CLVM_1$, both the segmentation and keypoint classifiers are defined on z_8 . For $CLVM_2$ and $M-CLVM_2$, z_1 is used for segmentation and z_5 for keypoints. To produce a segmentation, we take a max across all class predictions at each location. To produce keypoints, we take a max across all locations for each predicted heatmap. By thresholding the heatmap, our system can also detect keypoints.

4. Experiment Results

To evaluate our model, we ideally need benchmark datasets with both keypoint and pixel-level annotations, which are somewhat rare. We experiment with a single-task facial keypoint dataset (AFLW), a multi-task facial keypoint+pixel dataset (LFW-Part Labels) and a multi-task human-body keypoint+pixel dataset (Pascal Person). In all cases, we assume that detections are given, either making use of ground-truth bounding boxes or off-the-shelf detectors. We resize detection windows to 112×112 (padded to 180×180 for LFW-Parts to include the background) pixels before feeding into our models. We report an oracle upper bound computed from the ideal heat map, revealing the loss in accuracy due to spatial quantization. Recall that $CLVM_1$ is essentially a re-implementation of the bottom 8 layers of the state-of-the-art Deep19 CNN [42], and so represents quite a strong baseline. In all cases, we outperform both our baselines and prior art, sometimes approaching the oracle performance.

AFLW: The AFLW dataset [28] is a large-scale real-world collection of 25,993 faces in 21,997 real-world images, annotated with facial keypoints. We randomly select 1000 faces for validation, 1000 for testing, and the rest for training. Notably, these faces are not limited to be responses of an existing face detector, and so this dataset contains more pose variation than other landmark datasets. We hypothesized that such pose variation might still illustrate the benefit of bidirectional reasoning. We use the face detector of [55] to generate a rough bounding box labeling of each face. We refer the reader to Figure 7 for a summary of results, but our $CLVM$ models outperform state-of-the-art methods for facial keypoint estimation. In fact, even the bottom-up $CLVM_1$ outperforms the state-of-the-art, indicating the strength of the baseline. Our two-pass $CLVM_2$ reduces error by another factor of 2 with respect to the upper bound. These results reveal the potential benefit of bidirectional reasoning even for a single prediction task.

LFW-Parts: LFW Parts [24] contains 2,927 face images from widely-used the LFW face dataset [19] annotated with semantic pixel labels for Hair/Skin/Background (with standard train/val/test splits). We manually annotate keypoint locations by interactively applying and correcting the landmark detector trained from AFLW. We tabulate results

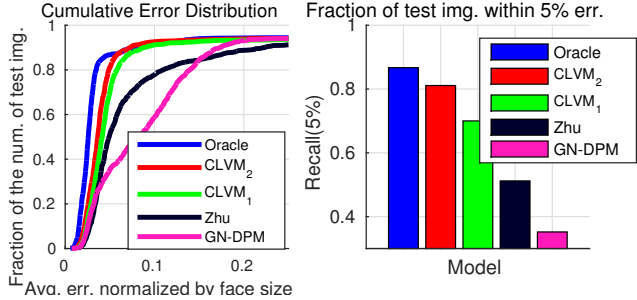


Figure 7: We plot average pixel localization error in AFLW, normalized by face size [55]. Because there are no segmentation labels, we compare only our single-task models $CLVM_1$ with $CLVM_2$ to recent state-of-the-art landmark localization systems (Zhu [55] and GN-DPM [46]). We learn a linear regressor to map the output of each method to a common subset of facial keypoints. The oracle upper-bound selects the minimum error location in the predicted heat map. We find that top-down feedback ($CLVM_2$) even helps for single-task prediction, producing a noticeable improvement that approaches the upper-bound.

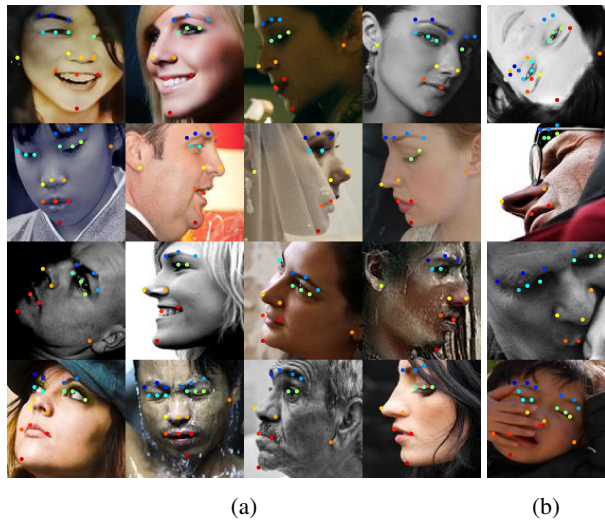


Figure 8: Facial landmark localization results of $CLVM_2$ on AFLW, where landmark ids are denoted by color. Our bidirectional model is able to deal with large variations in appearance, pose and illumination (a). We show images with extreme occlusions and pose variation in (b).

for pixel segmentation in Table 1 and keypoint location in Fig. 9. We refer the reader to the captions for a detailed analysis, but overall, we find that bidirectional top-down feedback is crucial for multi-task prediction, and that a single multi-task architecture performs as well (or even better than) multiple single-task architectures. In terms of segmentation, we reduce the best reported error [24] by a factor of 2. Fig. 10 visualizes qualitative results, while Fig. 11 and

Method	Accuracy (SP)	Error Reduction
CRF [24]	93.23%	0
Spatial CRF [24]	93.95%	10.64%
CRBM [24]	94.10%	12.85%
GLOC [24]	94.95%	25.41%
CLVM ₁	96.05%	41.60%
CLVM ₂	96.38%	46.60%
M-CLVM ₁	96.11%	42.59%
M-CLVM ₂	96.85%	53.48%
Oracle	99.97%	100.00%

Table 1: We plot superpixel-wise segmentation accuracy on LFW-Parts, following the protocol introduced in [24]. We show qualitative results in Fig. 10. We report both overall accuracy and error reduction with respect to a CRF baseline (as recommended by [24]). Our bottom-up baseline (CLVM₁) outperforms all published work. Adding top-down feedback (CLVM₂) improves results, while adding multi-task keypoint targets during learning (M-CLVM₂) produces the best overall performance. We further examine the latter model in Fig. 11 and Fig. 12.

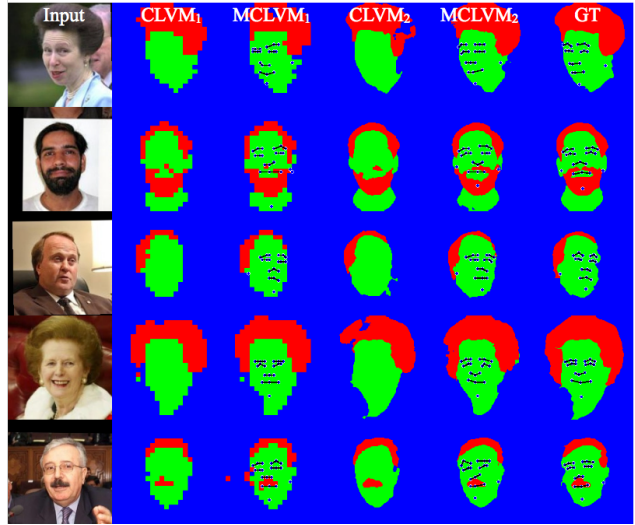


Figure 10: Segmentation and facial keypoint localization results on LFW-Parts. We use colors to denote hair (red), skin (green) and background (blue), and denote predicted keypoints with black dots. In general, bottom-up models CLVM₁ and M-CLVM₁ tend to predict pixelated segments because they use features from higher layers (that are highly nonlinear but spatially quantized). Adding top-down feedback (CLVM₂) tends to produce smoother segmentations, while multi-task training (M-CLVM₂) also removes spurious pixels.

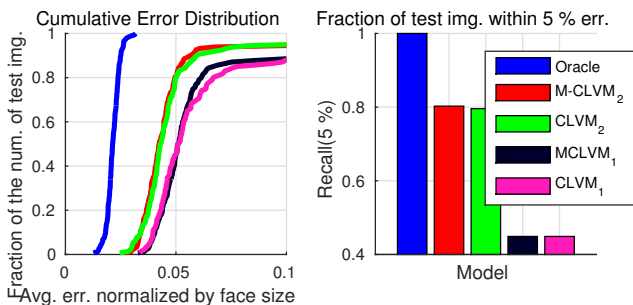


Figure 9: The **left** plots the cumulative error distribution for keypoint localization on LFW-Parts. The **right** plots the percentage of test images with an average localization error below 5%. Our two-pass models with feedback significantly outperform one-pass bottom-up variants. Multi-mask learning does not improve accuracy, but does improve speed (as we later show) because a single model can be used for diverse tasks.

Fig. 12 examine our best-performing model (M-CLVM₂) in detail.

Pascal Person: The Pascal 2011 Person dataset [14] consists of 7,368 person instances, each annotated with: (1) a bounding box around the visible region; (2) up to 23 human keypoints per person; and a (3) figure/ground segmentation mask. We randomly chose 70% for training, 10% for validation and 20% for testing. We evaluate localization accuracy of only visible keypoints, normalizing pixel error by the maximum side length of the instance’s visible bounding

box. We compare our model against state-of-the-art pose estimation systems [50] and [41], tuned to return their best detection given the visible bounding box. The performance of segmentation is shown in Table 2 and the performance of keypoint localization is shown in Figure 13. We show some sample results of the test set of Pascal Person in Figure 14. We refer the reader to the caption for a detailed analysis. Our CLVM models outperform prior art for keypoint localization by a large margin. Moreover, our bidirectional models strongly outperform their single-pass feedforward counterparts, particularly when evaluated on multitask prediction.

Convergence: As a diagnostic experiment, we verify that layer-wise coordinate updates do increase a global scoring function (Fig. 15). As we iterate beyond $k = 2$ passes (which is what the model was trained for), the score appears to grow unbounded, implying that the learned $(-W)$ is not PSD. We posit that more aggressive learning may ensure convergence - e.g., directly training a model with larger k , learning the regularization penalty (the main diagonal of W), and/or adding explicit constraints that enforce PSDness. Alternatively, one could redefine the global objective from (3) to include upper-bounds constraints on latent variables (through a saturating nonlinear activation function [15]).

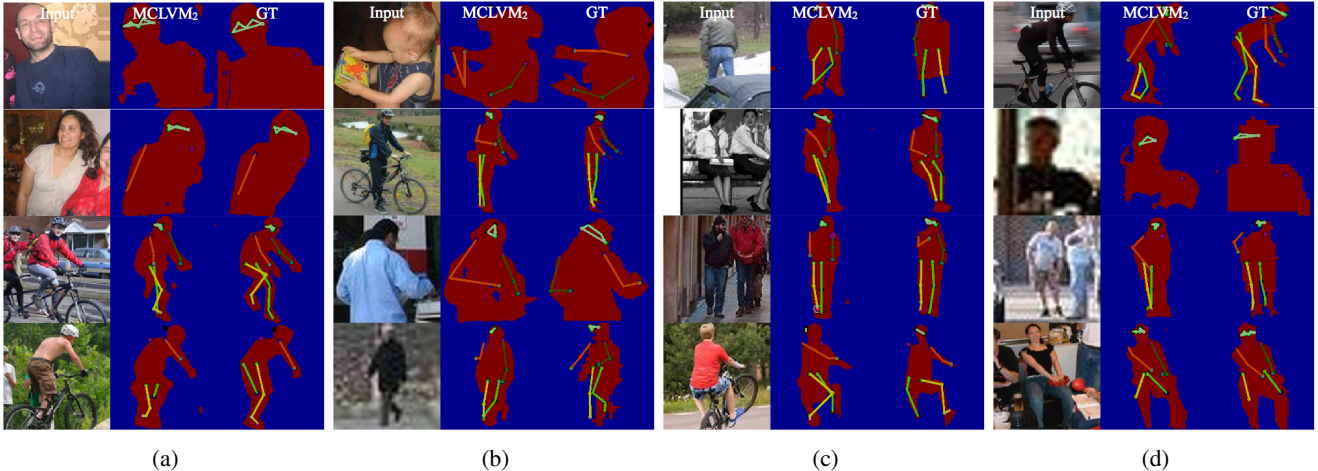


Figure 14: Sample segmentation and keypoint localization results on Pascal Person test set. Each subfigure has three columns: (1) original images; (2) predictions of segmentation masks and keypoint locations; (3) ground truth segmentation masks and visible human keypoints. We draw keypoints as skeletons. The bottom row of (c) and the top row of (d) show that our model can handle extreme poses, cluttered backgrounds and occlusions. The top row of (c) nicely illustrates the use of top-down information to help localize and segment a *fully-occluded* foot.

Method	Accuracy (P)
Oracle	99.53%
CLVM ₁	83.40%
CLVM ₂	86.56%
M-CLVM ₁	82.91%
M-CLVM ₂	86.57%

Table 2: Pixel-wise segmentation performance on Pascal Person. Our bidirectional models significantly outperform their bottom-up counterparts. Moreover, multi-task training slightly hurts our bottom-up model (CLVM₁ vs M-CLVM₁), but slightly helps our bidirectional model (CLVM₂ vs M-CLVM₂).

Weight-sharing: One could relax the recurrent CNN that implements our two-pass CLVM₂ model (Fig. 3) by not tying together weights across different layers. The un-tied network is strictly more flexible and can so can represent structures beyond latent-variable models. We found such models performed nearly identically to their tied counterparts while converging faster during training. Specifically, an untied M-CLVM₂ produced a super-pixel (SP) accuracy of 96.84% on LFW-Parts, just below M-CLVM₂’s performance of 96.85%, both of which are noticeably better than all other variants in Table 1. Such untied networks still provide a form of feedback, and so may be interesting to examine further.

Running time: We show the running time of our models in Table 3. As expected, multi-task prediction requires essentially no additional computation over single-task pre-

Model	Segmentation	Keypoint
CLVM ₁	15.5 ms	13.3 ms
CLVM ₂	31.0 ms	21.5 ms
M-CLVM ₁	16.1ms	
M-CLVM ₂	31.2ms	

Table 3: Running times for our model on a 180×180 image. Our two-pass (feedback-aware) models are 2X slower than their feedforward counterparts. Multi-task outputs essentially come “for free”. Our multi-task models are often 100-1000 faster than many of our *single-task* baselines.

diction (which is already quite fast). Our timing results are impressive given that many of the *single-task* baselines we compare against are 100-1000 times slower.

Conclusion: We have introduced a convolutional latent-variable model (CLVM) capable of bottom-up and top-down reasoning. CLVMs integrate several leading approaches, including CNNs, probabilistic Boltzmann machines, and discriminative latent-variable models. Both inference and learning are extremely efficient, making use of layer-wise updates that can be implemented with highly-optimized deep learning toolboxes. CLVMs produce rich multiscale features capable of supporting a diverse set of recognition tasks, including high-level keypoint localization and low-level pixel segmentation. We show that both high and low-level recognition can benefit from top-down feedback. Finally, we have demonstrated impressive performance, both in terms of accuracy and speed with respect to prior art.



Figure 11: Inspired by neurological experiments [32], we show low-level activations (3 out of 64 channels from Layer 1) at two different “times”. Columns correspond to activations on different images. The **top** row of each pair visualizes z'_1 (computed at 0.5ms, during bottom-up processing), while the **bottom** visualizes z_1 (computed at 30ms, after top-down feedback). The last column shows the average channel activation of both z'_1 and z_1 . Feedback captures figure-ground information corresponding to hair (Channel 7), skin (Channel 61), and background (Channel 33). Classifiers defined on such features produce better segmentations (Fig. 12).

Acknowledgments: Funding for this research was provided by NSF Grant 0954083, ONR-MURI Grant N00014-10-1-0933, and support from Intel. This research is also supported by the Office of the Director of National Intelligence (ODNI), Intelligence Advanced Research Projects Activity (IARPA), via IARPA R & D Contract No. 2014-14071600012. The views and conclusions contained herein are those of the authors and should not be interpreted as necessarily representing the official policies or endorsements, either expressed or implied, of the ODNI, IARPA, or the U.S. Government. The U.S. Government is authorized to reproduce and distribute reprints for Governmental purposes notwithstanding any copyright annotation thereon.

References

[1] D. H. Ackley, G. E. Hinton, and T. J. Sejnowski. A learning algorithm for boltzmann machines. *Cognitive science*, 9(1):147–169, 1985.

[2] E. Borenstein and S. Ullman. Combined top-down/bottom-up segmentation. *PAMI*, 30(12):2109–2125, 2008.

[3] T. Brox, L. Bourdev, S. Maji, and J. Malik. Object segmentation by alignment of poselet activations to image contours.

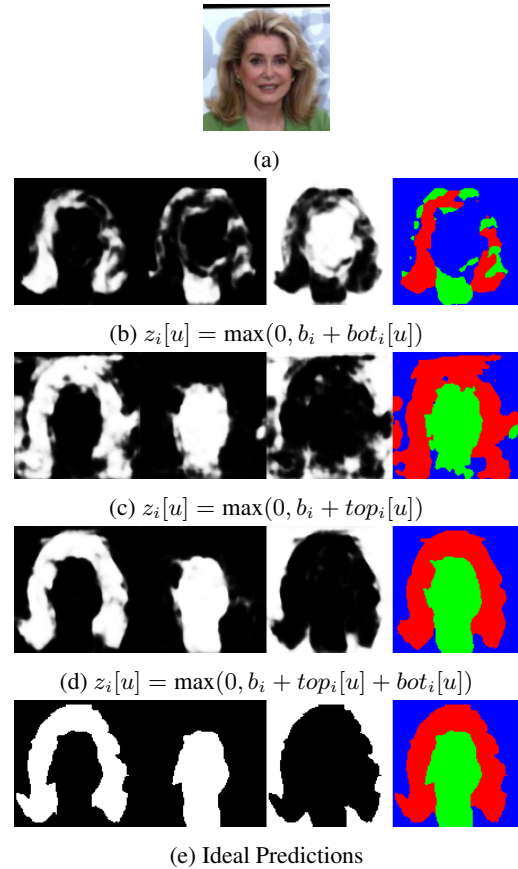


Figure 12: Hair, skin, and background pixel predictions obtained with the same softmax classifier applied to a bottom-up (b), top-down (c), and final combined (d) feature, contrasted with the ground truth (e). The overall segmentation mask for each feature is shown on the right. The top-down signal correctly estimates coarse spatial labels, but the bottom-up signals better respect image boundaries (but make gross errors, missing the entire face). The final predictions obtained by integrating both signals is the “best of both worlds.”

In *CVPR*, pages 2225–2232. IEEE, 2011.

[4] X. Chen and A. L. Yuille. Articulated pose estimation by a graphical model with image dependent pairwise relations. In *NIPS*, pages 1736–1744, 2014.

[5] R. J. Douglas, C. Koch, M. Mahowald, K. Martin, and H. H. Suarez. Recurrent excitation in neocortical circuits. *Science*, 269(5226):981–985, 1995.

[6] P. F. Felzenszwalb, R. B. Girshick, D. McAllester, and D. Ramanan. Object detection with discriminatively trained part-based models. *PAMI*, 32(9):1627–1645, 2010.

[7] V. Franc, V. Hlaváč, and M. Navara. Sequential coordinate-wise algorithm for the non-negative least squares problem. In *CAIP*, pages 407–414. Springer, 2005.

[8] R. Girshick, J. Donahue, T. Darrell, and J. Malik. Rich feature hierarchies for accurate object detection and semantic

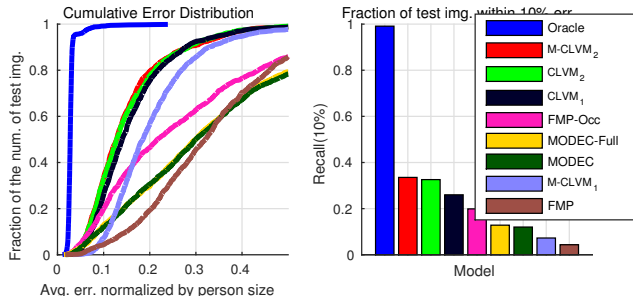


Figure 13: The **left** plot shows the cumulative error distribution for keypoints localization on Pascal Person. The **right** bar plot shows the percentage of test images that have average localization error below 10%. We evaluate localization accuracy of only visible keypoints, normalizing pixel error by the maximum side length of the instance’s visible bounding box. FMP and FMP-Occ are different versions of [50], where FMP-Occ has been re-trained on our training set. MODEC and MODEC-Full are two versions of models released by [41], where MODEC-Full is slower but better. Interestingly, multi-task learning significantly *hurts* our feed-forward models (CLVM₁ vs. M-CLVM₁), but slightly helps our bidirectional model (CLVM₂ vs. M-CLVM₂).

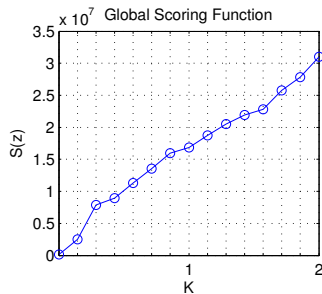


Figure 15: We plot the value of the global scoring function (3) as we perform iterations of layer-wise coordinate descent (6). Please see text for more discussion.

segmentation. In *CVPR*, pages 580–587. IEEE, 2014.

[9] R. Girshick, F. Iandola, T. Darrell, and J. Malik. Deformable part models are convolutional neural networks. *arXiv preprint arXiv:1409.5403*, 2014.

[10] X. Glorot, A. Bordes, and Y. Bengio. Deep sparse rectifier networks. In *AISTATS*, volume 15, pages 315–323, 2011.

[11] C. Goller and A. Kuchler. Learning task-dependent distributed representations by backpropagation through structure. In *ICNN*, volume 1, pages 347–352. IEEE, 1996.

[12] I. Goodfellow, M. Mirza, A. Courville, and Y. Bengio. Multi-prediction deep boltzmann machines. In *Advances in Neural Information Processing Systems*, pages 548–556, 2013.

[13] C. Gu, J. J. Lim, P. Arbeláez, and J. Malik. Recognition using regions. In *CVPR*, pages 1030–1037. IEEE, 2009.

[14] B. Hariharan, P. Arbeláez, L. Bourdev, S. Maji, and J. Malik. Semantic contours from inverse detectors. In *ICCV*, pages 991–998. IEEE, 2011.

[15] S. Haykin. *Neural networks and learning machines*, volume 3. Pearson Education Upper Saddle River, 2009.

[16] G. Hinton. Training products of experts by minimizing contrastive divergence. *Neural computation*, 14(8):1771–1800, 2002.

[17] G. E. Hinton, A. Krizhevsky, and S. D. Wang. Transforming auto-encoders. In *Artificial Neural Networks and Machine Learning–ICANN 2011*, pages 44–51. Springer, 2011.

[18] G. E. Hinton and R. R. Salakhutdinov. Reducing the dimensionality of data with neural networks. *Science*, 313(5786):504–507, 2006.

[19] G. B. Huang, M. Ramesh, T. Berg, and E. Learned-Miller. Labeled faces in the wild: A database for studying face recognition in unconstrained environments. Technical report, Technical Report 07-49, University of Massachusetts, Amherst, 2007.

[20] S. Ioffe and C. Szegedy. Batch normalization: Accelerating deep network training by reducing internal covariate shift. *arXiv preprint arXiv:1502.03167*, 2015.

[21] M. Ito and C. D. Gilbert. Attention modulates contextual influences in the primary visual cortex of alert monkeys. *Neuron*, 22(3):593–604, 1999.

[22] Y. Jin and S. Geman. Context and hierarchy in a probabilistic image model. In *CVPR*, volume 2, pages 2145–2152. IEEE, 2006.

[23] M. I. Jordan, Z. Ghahramani, T. S. Jaakkola, and L. K. Saul. *An introduction to variational methods for graphical models*. Springer, 1998.

[24] A. Kae, K. Sohn, H. Lee, and E. Learned-Miller. Augmenting crfs with boltzmann machine shape priors for image labeling. In *CVPR*, pages 2019–2026. IEEE, 2013.

[25] E. R. Kandel, J. H. Schwartz, T. M. Jessell, et al. *Principles of neural science*, volume 4. McGraw-Hill New York, 2000.

[26] A. Karpathy and L. Fei-Fei. Deep visual-semantic alignments for generating image descriptions. *arXiv preprint arXiv:1412.2306*, 2014.

[27] S. M. Kosslyn, W. L. Thompson, I. J. Kim, and N. M. Alpert. Topographical representations of mental images in primary visual cortex. *Nature*, 378(6556):496–498, 1995.

[28] M. Köstinger, P. Wohlhart, P. M. Roth, and H. Bischof. Annotated facial landmarks in the wild: A large-scale, real-world database for facial landmark localization. In *ICCV Workshops*, pages 2144–2151. IEEE, 2011.

[29] A. Krizhevsky, I. Sutskever, and G. E. Hinton. Imagenet classification with deep convolutional neural networks. In *NIPS*, pages 1097–1105, 2012.

[30] N. Kruger, P. Janssen, S. Kalkan, M. Lappe, A. Leonardis, J. Piater, A. J. Rodriguez-Sanchez, and L. Wiskott. Deep hierarchies in the primate visual cortex: What can we learn for computer vision? *PAMI*, 35(8):1847–1871, 2013.

[31] M. P. Kumar, P. H. Torr, and A. Zisserman. Objcut: Efficient segmentation using top-down and bottom-up cues. *PAMI*, 32(3):530–545, 2010.

[32] V. A. Lamme. The neurophysiology of figure-ground segregation in primary visual cortex. *The Journal of Neuroscience*, 15(2):1605–1615, 1995.

- [33] Y. LeCun, L. Bottou, Y. Bengio, and P. Haffner. Gradient-based learning applied to document recognition. *Proceedings of the IEEE*, 86(11):2278–2324, 1998.
- [34] T. S. Lee and D. Mumford. Hierarchical bayesian inference in the visual cortex. *JOSA A*, 20(7):1434–1448, 2003.
- [35] J. Long, E. Shelhamer, and T. Darrell. Fully convolutional networks for semantic segmentation. In *CVPR*. IEEE, 2015.
- [36] J. Masci, U. Meier, D. Cireşan, and J. Schmidhuber. Stacked convolutional auto-encoders for hierarchical feature extraction. In *Artificial Neural Networks and Machine Learning—ICANN 2011*, pages 52–59. Springer, 2011.
- [37] V. Nair and G. E. Hinton. Rectified linear units improve restricted boltzmann machines. In *ICML*, pages 807–814, 2010.
- [38] C. Peterson and J. Anderson. A mean field theory learning algorithm for neural networks. *Complex systems*, 1:995–1019, 1987.
- [39] A. S. Razavian, H. Azizpour, J. Sullivan, and S. Carlsson. Cnn features off-the-shelf: an astounding baseline for recognition. In *CVPR Workshop*, pages 512–519. IEEE, 2014.
- [40] R. Salakhutdinov and G. E. Hinton. Deep boltzmann machines. In *AISTATS*, pages 448–455, 2009.
- [41] B. Sapp and B. Taskar. Modec: Multimodal decomposable models for human pose estimation. In *CVPR*, 2013.
- [42] K. Simonyan and A. Zisserman. Very deep convolutional networks for large-scale image recognition. *arXiv preprint arXiv:1409.1556*, 2014.
- [43] R. Socher, C. C. Lin, C. Manning, and A. Y. Ng. Parsing natural scenes and natural language with recursive neural networks. In *ICML*, pages 129–136, 2011.
- [44] V. Stoyanov, A. Ropson, and J. Eisner. Empirical risk minimization of graphical model parameters given approximate inference, decoding, and model structure. In *International Conference on Artificial Intelligence and Statistics*, pages 725–733, 2011.
- [45] C. Szegedy, W. Liu, Y. Jia, P. Sermanet, S. Reed, D. Anguelov, D. Erhan, V. Vanhoucke, and A. Rabinovich. Going deeper with convolutions. *arXiv preprint arXiv:1409.4842*, 2014.
- [46] G. Tzimiropoulos and M. Pantic. Gauss-newton deformable part models for face alignment in-the-wild. In *CVPR*, pages 1851–1858. IEEE, 2014.
- [47] R. VanRullen and S. J. Thorpe. Is it a bird? is it a plane? ultra-rapid visual categorisation of natural and artificial objects. *Perception-London*, 30(6):655–668, 2001.
- [48] A. Vedaldi and K. Lenc. Matconvnet – convolutional neural networks for matlab. *CoRR*, abs/1412.4564, 2014.
- [49] P. Vincent, H. Larochelle, I. Lajoie, Y. Bengio, and P.-A. Manzagol. Stacked denoising autoencoders: Learning useful representations in a deep network with a local denoising criterion. *The Journal of Machine Learning Research*, 11:3371–3408, 2010.
- [50] Y. Yang and D. Ramanan. Articulated pose estimation with flexible mixtures-of-parts. In *CVPR*, pages 1385–1392. IEEE, 2011.
- [51] S. X. Yu and J. Shi. Segmentation given partial grouping constraints. *PAMI*, 26(2):173–183, 2004.
- [52] M. D. Zeiler and R. Fergus. Visualizing and understanding convolutional networks. In *Computer Vision—ECCV 2014*, pages 818–833. Springer, 2014.
- [53] M. D. Zeiler, D. Krishnan, G. W. Taylor, and R. Fergus. Deconvolutional networks. In *CVPR*, pages 2528–2535. IEEE, 2010.
- [54] L. L. Zhu, Y. Chen, and A. Yuille. Recursive compositional models for vision: Description and review of recent work. *Journal of Mathematical Imaging and Vision*, 41(1-2):122–146, 2011.
- [55] X. Zhu and D. Ramanan. Face detection, pose estimation, and landmark localization in the wild. In *CVPR*, pages 2879–2886. IEEE, 2012.
- [56] K. Zipser, V. A. Lamme, and P. H. Schiller. Contextual modulation in primary visual cortex. *The Journal of Neuroscience*, 16(22):7376–7389, 1996.